Crystal structures reveal the molecular basis of ion-translocation in sodium/proton antiporters

Mathieu Coincon[1,4], Povilas Uzdavinys[1,4], Emmanuel Nji[1], David L. Dotson[2], Iven Winkelmann[1], Saba Abdul-Hussein[1], Alexander D. Cameron[3], Oliver Beckstein[2], David Drew[1]

[1]Department of Biochemistry and Biophysics, Stockholm University, Stockholm, Sweden.

[2] Department of Physics and Center for Biological Physics, Arizona State University, Tempe, USA.

[3]School of Life Sciences, University of Warwick, Coventry, U.K.

[4]These authors contributed equally to the work

Correspondence should be addressed to D.D. (ddrew@dbb.su.se)

To fully understand the transport mechanism of Na^+/H^+ exchangers it is necessary to firmly establish the global rearrangements required to facilitate ion translocation. Currently, two different transport models have been proposed. Some reports suggest that structural isomerization is achieved through large, elevator-like rearrangements, similar to that seen in the structurally unrelated sodium-coupled glutamate transporter homologue Glt_{Ph}. Others have proposed that only small domain movements are required for ion exchange and a conventional rocking-bundle model has been proposed instead. Here, to resolve these differences we report atomic resolution structures of the same Na^+/H^+ antiporter (NapA from *Thermus thermophilus*) in both outward- and inward-facing conformations. These data combined with cross-linking, MD simulations and isothermal calorimetry strongly suggest that Na^+/H^+ antiporters provide alternating access to the ion-binding site using elevator-like structural transitions.

Na^+/H^+ exchangers (NHE1-9 in mammals) mediate the outward movement of protons (H^+) in exchange for sodium (Na^+) or lithium (Li^+) ions [1,2]. These transporters are important in regulating intracellular pH, sodium levels and cell volume, and in control of the cell cycle, cell proliferation, cell migration, and vesicle trafficking [1,2]. Na^+/H^+ exchangers belong to the monovalent cation:proton antiporter superfamily (CPA1-2), and are important drug targets, because their dysfunction is linked to a variety of diseases, including cancer and cardiovascular pathophysiology [2,3]. The Na^+/H^+ antiporter from *Escherichia coli* (NhaA), a bacterial homologue of the NHEs, was the first crystal structure of the CPA superfamily to be determined [4]. The structure revealed that Na^+/H^+ exchangers are made up of a central dimer domain and a core (ion-translocation) domain [4,5]. The core domain contains two anti-parallel discontinuous helices, TMs 4 and 11, which cross over near the centre of the protein. The ion-binding aspartate [4-8], ubiquitous among prokaryotic and eukaryotic Na^+/H^+ antiporters [1], is located on TM5, near the TM 4 and 11 crossover. In the crystal structure of NhaA [4], a negatively charged cavity is formed at the interface of

the two domains and provides access to the ion-binding aspartate from the cytoplasm. It was proposed that the two half-helices in the core domain would undergo small rearrangements to close access to the inside cavity and open the binding site to the outside [4,9]. However, recent comparisons to an outward-facing crystal structure of a homologous Na^+/H^+ exchanger, NapA from *T. thermophilus* [6], suggested that substrate translocation would rather occur by a large outward movement of the core domain itself. Because the size of the oligomerization surface in NapA is extensive (~1,800 $Å^2$), the core domain was modelled to move against a dimer domain that is fixed, yielding elevator-like movements similar to that seen in the trimeric sodium-coupled glutamate transporter homologue Glt_{Ph} [6 10].

Although an elevator-like model was proposed, a detailed mechanism could not be resolved because NhaA and NapA have relatively low sequence identity and show some structural differences[4-6], particularly in the dimer domain. Indeed these movements have been questioned in a more recent crystallographic study of the archaeal Na^+/H^+ antiporter NhaP1 from *Methanococcus jannaschii,* which has a similar topology to NapA[11]*. Mj*NhaP1 was solved in an inward-facing conformation by X-ray crystallography and the structure of the same protein in an outward-facing state using ~6/14-Å resolution electron microscopy (EM) maps obtained from 2D crystals[11]. Based on a comparison of these two structures it was concluded that the core domain undergoes much smaller movements, ruling out an elevator model and proposing the conceptually different rocking-bundle mechanism instead [11].

Since NhaA, NapA and NhaP1 proteins share low sequence identity to one another[6], the extent of rearrangements could differ between these proteins. Even so, the type of alternating-access model used by these and other Na^+/H^+ exchangers should be conserved. It seems that the current ambiguities are likely to only be resolved by the determination of equivalent or highly homologous Na^+/H^+ exchanger structures at near atomic resolution in both outward and inward facing states. To confirm the structural basis of ion-translocation in Na^+/H^+ exchangers we therefore set out to obtain a crystal structure of NapA in an inward-facing conformation.

RESULTS

Elevator-like movements of NapA can occur in a lipid bilayer

We hypothesised that if NapA undergoes elevator-like rearrangements, it should be possible to trap an inward-facing conformation by engineering a disulfide bond between a residue at position 31 in the dimer domain and a residue at position 130 in the core domain (Fig. 1a); in the outward-facing NapA structure these residues are located ~10 Å apart. To test this model, V31C and I130C mutants were constructed onto wild type NapA, which is cysteine-less, expressed in *E. coli* and purified at active pH (see Methods). Incubation of each of the single V31C and I130C mutants with maleimide-PEG-5k showed a clear species with higher electrophoretic mobility, indicating that both cysteine residues were solvent accessible (Fig. 1b and Supplementary Data Set 1). In contrast, incubation of maleimide-PEG-5k with the purified double cysteine V31C I130C mutant showed little pegylated product, indicating the same cysteine residues were no longer solvent accessible, presumably because they had formed a disulfide (Fig. 1b and Supplementary Data Set 1). Consistently, reactivity to a sulfhydryl binding dye was also significantly reduced in the double cysteine mutant as compared to each of the single cysteine mutants (see Methods and Supplementary Fig. 1a and Supplementary Data Set 1).

To determine if V31C and I130C residues are able to form a disulfide in a membrane environment, each of the purified cysteine mutants were co-reconstituted with *E. coli* F_0F_1 ATP synthase into liposomes (see Methods and Supplementary Fig. 1b). After establishment of a pH gradient by the addition of ATP, proton efflux was monitored in response to Na^+ or Li^+ addition in the presence of valinomycin and potassium. In the presence of DTT, single and double-cysteine mutants showed robust transporter activity with apparent Na^+ and Li^+ affinities (K_M) similar to that of wild type (Fig. 1 and Table 1). Likewise, after removal of DTT, wild type NapA and each of the single cysteine mutants showed similar antiport activities (Fig. 1c, d, g). In contrast, removal of DTT from proteoliposomes containing the double-cysteine mutant abolished ~90% of its transport activity (Fig. 1e, g). Re-addition of DTT restored antiport activity back to starting levels (Fig. 1e,

g). Thus, a disulfide bond between V31C in the dimer domain and I130C in the core domain can spontaneously form in a membrane environment, in agreement with an elevator-like transport model [6].

To provide further support for an elevator model we further engineered an SDS-resistant NapA dimer by covalently linking the two protomers together by substituting I55 with cysteine (Fig. 1a and Supplementary Fig. 1c and Supplementary Data Set 1). Consistent with a fixed dimer domain during transport the covalently linked dimer showed wild type-like antiport activity under either non-reducing or reducing conditions (Fig. 1g, Table 1 and Supplementary Fig. 1d).

The inward-facing crystal structure of NapA

Crystals of the cross-linked V31C I130C mutant were obtained, in the absence of any additional oxidizing reagents, and in similar crystallization conditions to that of the wild type NapA protein at active pH (Methods). The cross-linked V31C I130C mutant structure was solved by molecular replacement at 3.7 Å resolution (Fig. 2a and Table 2 and Supplementary Fig. 2a). The electron-density maps revealed that a disulfide bond has formed between residues C31 and C130 (Fig. 2b). In molecular dynamics (MD) simulations (Supplementary Table 1) the backbone r.m.s.d. increased to less than 3 Å over 1 μs, indicating that the disulfide-trapped structure is stable in a model membrane bilayer (Supplementary Fig. 3a). Similar r.m.s.d and r.m.s.f. fluctuations were also observed in MD when the disulfide was removed by the replacement of C31 and C130 with wild type residues (Supplementary Fig. 3a, b). Furthermore, the disulfide-trapped NapA structure superimposes well onto the inward-facing crystal structure of *Mj*NhaP1 (Supplementary Fig. 3c); the disulfide formed between residues C31 and C130 appears to have only caused a local conformational difference at the end of TM1. Strikingly, the strictly conserved ion-binding residues in NapA (D157) and *Mj*NhaP1 (D161) are positioned within only ~1 Å from one another (Supplementary Fig. 3c). As expected, the outward-facing cavity in NapA has closed and a vestibule has now opened to the inside (Fig. 2c).

Highly conserved residues are clearly surface exposed by the opening of the inward-facing cavity (Supplementary Fig. 3d).

The above discussion suggests that the introduction of the disulfide has not overly perturbed the NapA structure. As further corroboration we carried out isothermal titration calorimetry (ITC). As shown in Fig. 2d, the disulfide-locked protein is also able to bind Li^+ and Na^+ ions with affinities (K_d) in a similar range to their apparent K_M at pH 8 and 8.5, respectively (Table 1). Furthermore, NapA as with all Na^+/H^+ antiporters, shows strict pH dependent activity [12,13] and reflecting its pH-dependent transport activity[12], ion binding was also seen to be very pH sensitive (Fig. 2d). MD simulations of the inward-facing conformation further show how bulk Na^+ ions are able to access the strictly conserved ion-binding aspartate D157 from the cytoplasm (Supplementary Fig. 4a). In the simulation, D157 typically interacts with Na^+ in a bi-dendate configuration whereby both side chain oxygen atoms of the Asp are within less than 3 Å of the ion (Supplementary Fig. 4a–e and Supplementary Table 2). Coordination of Na^+ is similar to how thallium binds to the equivalent aspartate in the inward-facing NhaP structure from *Pyrococcus abyssi* [8]. In MD simulations, no dimer domain residues interacted with the Na^+ ion, consistent with the fact that the mutation of the poorly conserved dimer domain glutamate that was unexpectedly seen to also coordinate Tl^+ in *Pa*NhaP is not essential for transport [8]. We conclude that the disulfide-trapped structure of NapA is able to bind substrate and is in an inward-facing conformation, similar to that seen in homologous Na^+/H^+ antiporter structures [4,5,8,11].

Outward-facing NapA crystal structure in lipidic mesophase

Because the inward-facing NapA and *Mj*NhaP1 structures superimpose very well it is highly suggestive that they operate by a similar mechanism. Since the inward facing crystal structures are so similar (Supplementary Fig. 3c) the different mechanism proposed is likely a result of differences between the outward facing crystal structures. Indeed, the 2D structure of *Mj*NhaP1 based on the EM maps was reported to be less open to the outside than that seen in the outward-facing crystal structure of NapA [6,11]. It is possible that crystallization of NapA in detergent may

have contributed to the conformational differences observed between these two proteins [6].

To confirm that the outward-facing crystal structure of NapA represents a state that can also be populated in a lipid-bilayer, we engineered a different set of cysteine residues, between V71 in the dimer domain and L141 in the core domain; these residues are located ~15 Å apart in the inward-facing structure, but come within 5 Å of one another in the outward-facing structure (Supplementary Fig. 1e). As shown in Supplementary Fig. 1f-g, indeed, in the absence of DTT a disulfide bond is formed with ~90% efficiency between C71 and C141 residues in both detergent solution and in proteoliposomes (Supplementary Data Set 1). In the presence of DTT, however, the double V71C L141C mutant showed similar antiport activities to NapA wild type (Table 1 and Supplementary Fig. 1g). Lastly, we proceeded to combine 71C and 130C mutants as, unlike the previous pairings, they were modelled to remain at least ~10 Å apart in the two conformations and therefore should not be able to spontaneously form a disulfide bond (Supplementary Fig. 1e). Consistently, in proteoliposomes containing the 71C 130C mutant we observed little change in antiport activity upon the removal of DTT (Supplementary Fig. 1h).

To provide additional support for the physiological relevance of the outward-facing NapA crystal structure we further sought to obtain a structure of NapA at active pH using the lipidic-cubic phase (LCP) method (Fig. 3 and Table 2). Unlike the NapA crystal structure obtained in detergent, the structure refined at 2.3 Å resolution in lipids now shows bilayer-type crystal packing (Fig. 3b). Superimposition of the new outward-facing LCP crystal structure with that obtained in detergent[6] shows that the core domain has still, nonetheless, adopted the same overall conformation (Fig. 3a). The main difference between the two outward-facing structures is that the half-helices 11b and 4a have tilted ~6 Å further away from the cavity in the LCP structure, which makes it more open (Fig. 3a). This difference might be due to the involvement of these helices in crystal packing (Fig. 3b). In MD simulations, half-helices 11b and 4a fluctuate between the positions seen in both outward-facing NapA crystal structures, indicating that they are very mobile (Fig. 3c). The open vestibule in the LCP structure provides an open path for Na^+ ions to

bind to D157 from the extracellular solvent (Supplementary Fig. 4f-i). Although binding events are infrequent and short (Supplementary Fig. 4j), they nevertheless show ion coordination geometry similar to that observed in the inward-facing conformation (Supplementary Fig. 4a–e and Supplementary Table 2).

An Elevator alternating-access mechanism for Na^+/H^+ antiport

Based on the fact that the dimer domain is held in place by its interaction with the other protomer it seems reasonable to assume that the core domain moves against the dimer domain, i.e., rather than the dimer moving against the core. To test this assumption we carried out MD simulations of the outward- and inward facing NapA crystal structures in a model membrane bilayer (Supplementary Table 1). While the vertical position (*z* coordinate) of the dimer domain in the membrane only differed by ~2 Å between outward and inward facing conformation, the core domain moved ~6 Å relative to the membrane and ~7 Å relative to the position of the dimer domain (Supplementary Fig. 5). Thus, the core domain is able to move freely against a dimer domain that can anchor the position of the transporter in the membrane.

A morph between the outward and inward-facing NapA crystal structures shows that, whilst the dimer domain only breathes out side-ways, the core domain undergoes a large rotation and a translation (Methods and Supplementary Videos 1 and 2). During this rearrangement the Cα atom of the ion-binding aspartate (D157) is re-located ~8 Å in the vertical direction (Supplementary Fig. 2b, c). The side-chain of D157 further rotates some 55°, which is necessary for the residue to access the inward-facing vestibule (Fig. 2c and Supplementary Fig. 2c). The distance between the D157 carboxylate groups in the two opposite-facing states is ~11 Å (Fig. 4b and Supplementary 2b). This ion-binding site re-location spans a distance that is roughly equivalent to the thickness of the hydrophobic dimer domain interface (Fig. 4a). The elevator-like movement of the core against the dimer domain is facilitated by long flexible loops that are located between TMs 9 and 10 on the extracellular side, and between TM6 and 7 on the intracellular side (see Methods and Supplementary Fig. 6). These hinge regions contain a number of glycine residues G193, G213, G277 and

G294, which may facilitate the unwinding of the helices at their connecting periphery. The hinge regions are clearly highlighted when the higher-resolution outward-facing (LCP) NapA structure is represented by temperature factors (Supplementary Fig. 6b). These hinge regions also show high per-residue fluctuations in MD simulations (Supplementary Fig. 3b).

Between the outward and inward-facing NapA conformations there is remarkably little structural rearrangement within the core and dimer domain themselves, as separate superimposition of the domains yields a root mean square deviation (r.m.s.d.) of 0.5 Å for 124 pairs of Cα atoms of the dimer domain and ~1.0 Å for 185 pairs of Cα atoms in the core domain (Fig. 4c). Within the core domain, residues located on the mobile TM4b and TM11b half-helices make most of the contacts to the dimer domain, which are extensive enough to close off the cavity to the outside and inside, respectively (see Methods and Fig. 5a, b). The small size of the occluding interface is clearly observed when TM4b and TM11b half-helices are omitted in a surface representation of NapA (Fig. 5a). Positively charged residues K344 in TM11b and R133 in TM4b may help to stabilise the alternate conformations by interacting with negatively charged residues on the dimer domain (Fig. 5b). Indeed, a K344A mutant has a clear negative effect on transport activity, as does the mutation of the intracellular R133 E35 salt-bridge between TM4b and TM1, which can be rescued by a charged-swapped mutant (Fig. 5c and Table 1). As extensively shown, ion binding catalyses the rearrangement of half-helices in the core domain [11,14,15]. It is likely that in the presence of Na^+ (Li^+) the mobile TM4b and TM11b helices move to further accommodate the substrate so that they are no longer interacting with the dimer domain, thus enabling the core to move in an elevator-like fashion as described. Interestingly, in the outward-facing LCP structure a number of acyl chains, modelled as LCP lipids, are located between the TM4b and TM11b half-helices and the dimer domain (Fig. 3a and Supplementary Fig. 7a). It is plausible that *in vivo* lipids may help to grease the elevator-like structural transitions of the core domain. Such an idea has also been proposed to facilitate transport domain movements in the glutamate transporter homologue Glt_{Ph} [16].

DISCUSSION

Na^+/H^+ antiporters have been extensively studied since West and Mitchell showed in the 1970's that H^+ and Na^+ transport could be strictly coupled[17]. With exchange activity in the milli- to microsecond time-scales, Na^+/H^+ antiporters represent one of the fastest known classes of secondary-active transporters [8,11,18]. At active pH, biophysical and biochemical data support an antiport mechanism whereby $Na^+(Li^+)$ compete with protons for a single binding site[7,19-21], which is made up of a strictly conserved aspartic acid and several other polar residues[1,2,4-8,21].

What has been unclear is the structural basis for the ion-exchange mechanism. Based on a comparison of the inward-facing structure of NhaA and the outward-facing structure of NapA we suggested that they would work by an elevator-like transport mechanism[6]. Elevator mechanisms were first described for the sodium-coupled glutamate transporter homologue Glt_{Ph}[10] and have since been proposed for various other transporters [22,23,24,25,26] including the bacterial sodium coupled bile acid transporter homologues, which have the same fold as the Na^+/H^+ antiporters[27,28]. The characteristic of this mechanism is that one domain undergoes a large, essentially, rigid-body movement against the other to carry the substrate across the membrane. This differentiates the mechanism from the rocking-bundle mechanism where the two domains move around the bound substrate (Fig. 6). Thus, an elevator-like mechanism requires a large conformational change and a vertical displacement of the substrate-binding site.

A comparison of the outward and inward structures of *Mj*NhaP1 shows only a small change[11]. Indeed, when the dimer domains of the two structures are superimposed the Cα atom of Asp161 is displaced vertically by only 1.5 Å (Supplementary Fig. 7b), which is much smaller than the 10 Å predicted from our previous model[6]. In this study we have trapped NapA in an inward-facing conformation through the introduction of a disulfide bond that gave rise to a crystal structure that is similar to the inward-facing crystal structure of *Mj*NhaP1[11]. We could further show that the disulfide-locked inward-facing NapA mutant is able to bind Na^+ and Li^+ ions in a pH specific manner with measured K_ds similar to the

respective apparent K_Ms. A comparison of this structure with outward-facing structure of NapA (determined from crystals grown in either detergent or lipid) confirms and refines the large elevator-like structural transitions. The difference between the two studies lies predominantly with the conformation of the outward-facing structure where that derived for *Mj*NhaP1 from the low resolution EM maps was modelled to be much less open than that seen in NapA[11]. Because side-chains cannot be modelled at this resolution it is not possible to ascertain whether the ion-binding site in *Mj*NhaP1 is accessible to the outside. Further, since this structure was determined at inactive pH[11], it may have affected the structure of the ion-binding site and possibly the conformation of the core domain. Indeed, pH dependent structural differences have been reported in Na^+/H^+ antiporters including *Mj*NhaP1 [8,14,29,30].

It seems likely that the overall rearrangements described here for NapA will be similar in other Na^+/H^+ exchangers, as we were able to predict with reasonable accuracy the inward-facing conformation of NapA using the inward-facing NhaA crystal structure[4]. Indeed, the extent of core movement is very similar to the elevator-like rearrangements described for bacterial sodium coupled bile acid transporter homologues, despite the fact that they operate at much slower turnover rates[28].

Because a Na^+ or Li^+ bound structure of a Na^+/H^+ antiporter is yet to be determined, intermediate and possibly occluded ion-bound states have yet to be experimentally resolved. It seems likely that additional structural changes not yet seen in crystal structures or MD simulations are likely to take place. These states will be important for understanding the coupling between conformational states and transport rates. What we do know is that numerous studies including cysteine accessibility analysis, tryptophan quenching and 2D crystallography support the local movement of the half-helices at active pH and/or upon the addition of substrate [15,31,32]. We propose that these ion- and/or proton-induced rearrangements will be a prerequisite for catalyzing the large structural changes observed here and, as seen in NapA, may further require the breakage of inter domain salt-bridges. It is tempting to further speculate that the core domain itself does not readily move

against the hydrophobic “barrier” of the dimer domain interface surface in the absence of substrate, because of its “non-filled” negatively charged ion-binding surface (Fig. 4a).

Although clearly more studies are required to elucidate the finer coupling of ion-binding with the global conformational changes described here, we have nonetheless demonstrated fresh atomic-level insights into how an ion exchanger can use large, elevator-like structural transitions to translocate ions across a lipid bilayer.

ACCESSION CODES

The coordinates and the structure factors for NapA have been deposited in the Protein Data Bank with entries 5BZ2 (inward-facing) and 5BZ3 (LCP outward-facing).

ACKNOWLEDGEMENTS

We are grateful to G. Verdon for discussions and comments. Data were collected at Diamond Light Source with excellent assistance from beamline scientists. This work was supported by the Swedish Research Council (D.D.) and the Knut and Alice Wallenberg Foundation (D.D). The authors are grateful for the use of the Membrane Protein Laboratory supported by the Wellcome Trust U.K. (grant 062164/Z/00/Z) at the Diamond Light Source Limited and The Centre for Biomembrane Research supported by the Swedish Foundation for Strategic Research. Computer simulations were partially run on the Extreme Science and Engineering Discovery Environment (XSEDE), which is supported by National Science Foundation grant OCI-1053575 (allocation TG-MCB130177, to O.B.). M.C was supported as a Wenner-Gren postdoctoral fellow and D.D. is supported as a European Molecular Biology Organization (EMBO) Young Investigator.

AUTHOR CONTRIBUTIONS

D.D. designed the project. Cloning, expression screening, protein purification and crystallisation of inward-facing NapA was carried out by M.C and P.U. LCP

crystallization of outward-facing NapA was carried out by E.N. Data collection and structural determination were carried out by M.C and D.D with assistance from E.N and A.C. Experiments for functional analysis were carried out by P.U., I.W., S.H and M.C. MD simulations were carried out by D.L.D. and O.B. D.D. wrote the manuscript with contributions from all authors.

COMPETITING FINANCIAL INTERESTS

The authors declare no competing financial interests.

References

1. Brett, C.L., Donowitz, M. & Rao, R. Evolutionary origins of eukaryotic sodium/proton exchangers. *Am J Physiol Cell Physiol* **288**, C223-39 (2005).
2. Fuster, D.G. & Alexander, R.T. Traditional and emerging roles for the SLC9 Na^+/H^+ exchangers. *Pflugers Arch* **466**, 61-76 (2014).
3. Verma, V., Bali, A., Singh, N. & Jaggi, A.S. Implications of sodium hydrogen exchangers in various brain diseases. *J Basic Clin Physiol Pharmacol* (2015).
4. Hunte, C. et al. Structure of a Na^+/H^+ antiporter and insights into mechanism of action and regulation by pH. *Nature* **435**, 1197-202 (2005).
5. Lee, C. et al. Crystal structure of the sodium-proton antiporter NhaA dimer and new mechanistic insights. *J Gen Physiol* **144**, 529-44 (2014).
6. Lee, C. et al. A two-domain elevator mechanism for sodium/proton antiport. *Nature* **501**, 573-7 (2013).
7. Maes, M., Rimon, A., Kozachkov-Magrisso, L., Friedler, A. & Padan, E. Revealing the Ligand Binding Site of NhaA Na^+/H^+ Antiporter and its pH Dependence. *J Biol Chem* (2012).
8. Wohlert, D., Kuhlbrandt, W. & Yildiz, O. Structure and substrate ion binding in the sodium/proton antiporter PaNhaP. *Elife* **3**, e03579 (2014).
9. Arkin, I.T. et al. Mechanism of Na^+/H^+ antiporting. *Science* **317**, 799-803 (2007).
10. Reyes, N., Ginter, C. & Boudker, O. Transport mechanism of a bacterial homologue of glutamate transporters. *Nature* **462**, 880-5 (2009).
11. Paulino, C., Wohlert, D., Kapotova, E., Yildiz, O. & Kuhlbrandt, W. Structure and transport mechanism of the sodium/proton antiporter MjNhaP1. *Elife* **3**, e03583 (2014).
12. Furrer, E.M., Ronchetti, M.F., Verrey, F. & Pos, K.M. Functional characterization of a NapA Na(+)/H(+) antiporter from *Thermus thermophilus*. *FEBS Lett* **581**, 572-8 (2007).
13. Padan, E. et al. NhaA of *Escherichia coli*, as a model of a pH-regulated Na+/H+antiporter. *Biochim Biophys Acta* **1658**, 2-13 (2004).
14. Kozachkov, L. & Padan, E. Conformational changes in NhaA Na(+)/H(+) antiporter. *Mol Membr Biol* (2012).
15. Rimon, A., Kozachkov-Magrisso, L. & Padan, E. The unwound portion dividing helix IV of NhaA undergoes a conformational change at physiological pH and lines the cation passage. *Biochemistry* **51**, 9560-9 (2012).
16. Akyuz, N. et al. Transport domain unlocking sets the uptake rate of an aspartate transporter. *Nature* **518**, 68-73 (2015).
17. West, I.C. & Mitchell, P. Proton/sodium ion antiport in *Escherichia coli*. *Biochem J* **144**, 87-90 (1974).
18. Taglicht, D., Padan, E. & Schuldiner, S. Overproduction and purification of a functional Na^+/H^+ antiporter coded by nhaA (ant) from *Escherichia coli*. *J Biol Chem* **266**, 11289-94 (1991).

19. Mager, T., Rimon, A., Padan, E. & Fendler, K. Transport mechanism and pH regulation of the Na^+/H^+ antiporter NhaA from *Escherichia coli*: an electrophysiological study. *J Biol Chem* **286**, 23570-81 (2011).
20. Calinescu, O., Paulino, C., Kuhlbrandt, W. & Fendler, K. Keeping it simple, transport mechanism and pH regulation in Na^+/H^+ exchangers. *J Biol Chem* **289**, 13168-76 (2014).
21. Calinescu, O., Danner, E., Bohm, M., Hunte, C. & Fendler, K. Species differences in bacterial NhaA Na^+/H^+ exchangers. *FEBS Lett* **588**, 3111-6 (2014).
22. Cao, Y. et al. Crystal structure of a phosphorylation-coupled saccharide transporter. *Nature* **473**, 50-4 (2011).
23. Luo, P. et al. Crystal structure of a phosphorylation-coupled vitamin C transporter. *Nat Struct Mol Biol* **22**, 238-41 (2015).
24. Johnson, Z.L., Cheong, C.G. & Lee, S.Y. Crystal structure of a concentrative nucleoside transporter from *Vibrio cholerae* at 2.4 Å. *Nature* **483**, 489-93 (2012).
25. Bolla, J.R. et al. Crystal structure of the *Alcanivorax borkumensis* YdaH transporter reveals an unusual topology. *Nat Commun* **6**, 6874 (2015).
26. Su, C.C. et al. Structure and function of *Neisseria gonorrhoeae* MtrF illuminates a class of antimetabolite efflux pumps. *Cell Rep* **11**, 61-70 (2015).
27. Hu, N.J., Iwata, S., Cameron, A.D. & Drew, D. Crystal structure of a bacterial homologue of the bile acid sodium symporter ASBT. *Nature* **478**, 408-11 (2011).
28. Zhou, X. et al. Structural basis of the alternating-access mechanism in a bile acid transporter. *Nature* **505**, 569-73 (2014).
29. Vinothkumar, K.R., Smits, S.H. & Kuhlbrandt, W. pH-induced structural change in a sodium/proton antiporter from M*ethanococcus jannaschii*. *EMBO J* **24**, 2720-9 (2005).
30. Paulino, C. & Kuhlbrandt, W. pH- and sodium-induced changes in a sodium/proton antiporter. *Elife* **3**, e01412 (2014).
31. Kozachkov, L. & Padan, E. Site-directed tryptophan fluorescence reveals two essential conformational changes in the Na^+/H^+ antiporter NhaA. *Proc Natl Acad Sci U S A* **108**, 15769-74 (2011).
32. Appel, M., Hizlan, D., Vinothkumar, K.R., Ziegler, C. & Kuhlbrandt, W. Conformations of NhaA, the Na^+/H^+ exchanger from *Escherichia coli*, in the pH-activated and ion-translocating states. *J Mol Biol* **388**, 659-72 (2009).
33. Yernool, D., Boudker, O., Jin, Y. & Gouaux, E. Structure of a glutamate transporter homologue from P*yrococcus horikoshii*. *Nature* **431**, 811-8 (2004).

Figure Legends

Fig. 1. **Disulfide-trapping of NapA in an inward-facing conformation a.** Cartoon representation of the outward-facing NapA structure (one of the protomers is faded). Core (ion-translocation) domain is shown in blue, the dimer domain in wheat, and the linker helix (TM6) in grey. Residues used for cysteine mutagenesis are depicted in stick and colour coded (V31 red, I55 blue and I130 green). **b.** The degree of cysteine reactivity of wild type NapA (WT), single and double cysteine mutants (open circle) to maleimide-PEG-5k (black circle) **c.**, **d.**, and **e.** Typical ACMA fluorescence traces of proteoliposomes containing single and double cysteine NapA mutants in the presence of DTT (reducing, black trace), after the removal of DTT (non-reducing, red trace) and after the re-addition of DTT (re-reducing, blue trace).

Each experiment was independently repeated 3 times. Note: the ΔpH gradient established between 0-3 min is not shown (see Supplementary Fig. 1b). **f.** The apparent K_M for Na^+ (filled circles) and Li^+ (open circles) of the double cysteine mutant under reducing conditions. The apparent (Na^+) and (Li^+) K_M affinities were calculated with a range of ion concentrations that were fitted by non-linear regression using data from two technical repeats (error bars show the spread of two data points and the values reported are the mean ± s.e.m. of the fit; see also Table 1). **g.** Quantification of antiport activity after the addition of LiCl in the presence (reducing) or absence (non-reducing) of DTT (error bars, s.e.m. from n = 3 experiments).

Fig. 2 The disulfide-trapped structure of NapA in an inward-facing conformation. a. NapA monomer (core blue; dimer wheat) shown in the outward-facing conformation (left, PDB: 4bwz) and inward-facing conformation (right, V31C-I130C). Positions of the V31 and I130 residues substituted with cysteine (left) are shown in red and green stick form, respectively. The ion binding aspartate D157 is shown in stick form (orange). **b.** Simulated-annealing FoFc omit map at 3.5σ of the disulfide formed between C31 and C130 residues in the inward-facing structure. **c.** Surface representation of the NapA structures clipped through the ion binding sites in either the outward-facing (left) or inward-facing (right) conformation. The strictly conserved ion-binding aspartate D157 is shown in stick form (orange) and labelled. **d.** Representative ITC thermogram obtained by successive addition of Li^+, K^+ or Na^+ to the V31C I130C mutant under non-reducing conditions (see Methods). Integrated heats with baseline-subtracted (red line) inverted power data are shown in top panels. Fit of a single binding site with 1:1 stoichiometry is shown in bottom panels (black line). Values of the K_d reported are the mean ± s.e.m. of the fit.

Fig. 3 LCP structure of NapA supports the physiological positioning of the outward-facing conformation. a. Electrostatic surface representation of NapA protomer from outward-facing structure obtained by vapor-diffusion (left) and

lipidic cubic phase (middle), as viewed from the extracellular side. Cartoon representation of the NapA outward-facing structure obtained by vapour-diffusion (dimer grey; core blue) superimposed on the outward-facing LCP structure (dimer brown and core teal) (left). The position of the ion-binding site is circled and additional and non-protein density at the core-dimer domain interface modelled as the LCP lipid MAG7.7 (green sticks). **b**. Ribbon representation of outward-facing NapA structure crystallized in the lipidic mesophase. One NapA dimer structure is shown in yellow and TM11b, likely to form crystal-packing contacts, is shown in red. **c**. View on the extracellular face (top panel) and inward facing face (bottom panel) of NapA. Conformations from a 1μs-MD simulation (cyan) of the LCP structure (yellow) and the detergent structure (PDB id 4BWZ; pink) as described in Methods. Representative snapshots of the mobile half-helices TM 4a and 11b are shown at varying time points (0 ns to 1000 ns) and are highlighted by a red dotted circle.

Fig. 4 An elevator-like alternating-access mechanism for Na^+/H^+ antiport. a. The outward-facing NapA structure was separated into core and dimer domains, and the electrostatic surface of the core (left) and dimer (middle) domain rendered. The view shows the domain surfaces that face one another at the interface. The electrostatic surface was further rendered for the inward-facing conformation (right) and shown based on its relative position to the dimer domain. The ion-binding aspartate D157 is represented as a green and yellow sphere for the outward-facing (left) and inward-facing (right) conformations, respectively. Dashed lines represent the position of the aspartate in each of the two conformations (middle) **b.** Cartoon representation highlighting the movement of the core domain (dark blue) between outward-facing (left) and inward-facing (right) conformations. The ion-binding aspartate D157 is shown as a sphere in the outward-facing (green) and inward-facing (yellow) conformations. **c**. The core and dimer domains from the different NapA crystal structures were superimposed separately onto each other. Left: outward-facing detergent structure (dimer dark-brown; core dark-blue) onto outward-facing LCP structure (dimer grey; core teal). Middle: outward-facing LCP structure (dimer grey; core teal) onto inward-facing NapA structure (dimer light-

orange; core light-blue). Right: outward-facing detergent structure (dimer dark-brown; core dark-blue) onto inward-facing NapA structure (dimer light-orange; core light-blue). The respective Cα-r.m.s.d. of each superimposition is shown.

Fig. 5 The cavity closing interactions formed between the Dimer and Core domains. **a**. The NapA surface (blue core; wheat dimer) shown in either the inward-facing (left) or outward-facing (right) conformation. Half-helices TM11b (orange) and TM4b (magenta) are further illustrated in cartoon in the left protomer of each dimer. **b**. Ribbon representation of NapA (blue core; wheat dimer) in inward-facing (left) or outward-facing (right) conformation. The alternating ionic interactions between the dimer domain and core helices TM11b (orange) and TM4b (mangeta) are highlighted (green sticks). **c**. Kinetic analysis of a salt-bridge swap between residues E35R in TM11b and R133E in the dimer domain. The apparent (Na^+) K_M affinities were calculated with a range of ion concentrations that were fitted by non-linear regression using data from two technical repeats (error bars show the spread of two data points and values reported are the mean ± s.e.m. of the fit; see also Table 1).

Fig. 6 Schematic illustrating the conceptual differences between "rocking-bundle" and "elevator" alternating-access mechanisms a. In the "rocking-bundle" alternating-access mechanism the substrate (red circle) binds between two similar sized domains (light orange) near the center of the membrane, which catalyzes their rearrangement around the substrate. **b.** In the "elevator" alternating access mechanism the substrate (red circle) binds predominantly or exclusively to only one of the domains (light orange), which is then carried across the membrane against the fixed, oligomerization domain (dark orange). The vertical displacement of the substrate between the two alternative conformations (relative to the scaffold domain) is likely to be in the range of ~10 to 18 Å as seen in NapA[6] and Glt_{Ph}[10,33] structures, respectively. For sake of simplicity, intermediate and occluded states

formed between the two major outward- and inward-facing conformations are not shown.

Table 1

Biochemical characterization of NapA mutants.

The apparent (Na^+) and (Li^+) K_M affinities were calculated with range of ion concentrations (n = 10) that were fitted by non-linear regression using data from two technical repeats (values reported are the mean ± s.e.m. of the fit). For the double-cysteine mutants the transport kinetics were measured in the presence of 5 mM DTT.

NapA	K_M (mM) at pH = 8.0	
	Na^+	Li^+
WT	2.08 ± 0.12	0.56 ± 0.02
V31C	1.48 ± 0.14	0.27 ± 0.04
I130C	6.14 ± 0.83	0.55 ± 0.06
V31C I130C	4.74 ± 0.38	0.64 ± 0.08
V31C I130C*	4.89 ± 0.65	
I55C	2.20 ± 0.10	0.44 ± 0.03
V71C L141C	6.46 ± 0.47	0.49 ± 0.04
R133E	9.33 ± 1.56	2.64 ± 0.50
E35R	> 50	3.22 ± 0.87
R133E E35R	5.87 ± 0.35	1.22 ± 0.20
K344A	14.60 ± 2.00	2.31 ± 0.32

*The apparent affinity K_M for V31C I130C was also measured for Na^+ at pH 8.5.

Table 2 Data collection and refinement statistics (molecular replacement)

	LCP	V31C I130C
Data collection		
Space group	C 2 2 21	C 2 2 21
Cell dimensions		
a, *b*, *c* (Å)	56.58, 94.09, 147.28	77.71,84.64,201.78
α, β, γ (°)	90, 90, 90	90, 90, 90
Resolution (Å)	47.04 - 2.3 (2.382 - 2.3) [a]	33.64 - 3.7 (3.832 - 3.7)
R_{merge}	0.182 (1.036)	0.090 (2.788)
CC 1/2	0.972 (0.735)	0.999 (0.575)
*CC**	0.993 (0.921)	0.999 (0.854)
$I / \sigma I$	12.24 (1.65)	13.26 (1.13)
Completeness (%)	99 (100)	100 (100)
Redundancy	4.5(4.5)	12.7 (13.3)
Refinement		
Resolution (Å)		
No. reflections	17750	7386
R_{work} / R_{free}	0.206 / 0.218	0.292 / 0.325
No. atoms		
Protein	2828	2823
Ligand	147	-
Water	76	-
B factors		
Protein	45.5	197
Ligand	72.8	-
Water	50.4	-
r.m.s. deviations		
Bond lengths (Å)	0.005	0.005
Bond angles (°)	0.96	0.81
Number of TLS group	-	1

[a] Values in parentheses are for highest-resolution shell.

ONLINE METHODS

Materials and Methods: *Thermus thermophilus* NapA sequence (Uniprot accession number Q72IM4); residues substituted to cysteine in the disulfide-trapped inward-facing NapA structure are underlined, and additional C-terminal residues retained after TEV cleavage are shown in italics.

MHGAEHLLEIFYLLLAAQVMAFIFKRLNQPVVIGEVLAGVLVGPALLGLVHEGEILEFLAEL
GAVFLLFMVGLETRLKDILAVGKEAFLVAVLGVALPFLGGYLYGLEIGFETLPALFLGTALV
ATSVGITARVLQELGVLSRPYSRIILGAAVIDDVLGLIVLAVVNGVAETGQVEVGAITRLIVLS
VVFVGLAVFLSTLIARLPLERLPVGSPLGFALALGVGMAALAASIGLAPIVGAFLGGMLLSE
VREKYRLEEPIFAIESFLAPIFFAMVGVRLELSALASPVVLVAGTVVTVIAILGKVLGGFLGA
LTQGVRSALTVGVGMAPRGEVGLIVAALGLKAGAVNEEEYAIVLFMVVFTTLFAPFALKPL
IAWTERERAAKE*GSENLYFQ*.

Protein expression and purification. NapA wild type was previously cloned into the vector pWaldoGFPe, which harbours a TEV cleavable C-terminal GFP-His_8 tag, and mutants were generated from this vector[6] using the Quickchange protocol (Agilent Technologies). NapA wild type and mutants were transformed into the *E. coli* strain Lemo21(DE3)[34] and overexpressed following the MemStar protocol [35].

Membranes containing overexpressed fusions were isolated from 6 l *E. coli* cultures and solubilized in 1% w/v dodecyl-β-D-maltopyranoside (DDM; Generon) for 1 h in buffer containing 1 x PBS and 150 mM NaCl. The suspension was cleared by ultracentrifugation at 200,000 *g* for 1 h. The cleared supernatant was incubated with 1 ml of Ni-NTA Superflow resin (Qiagen) per 1 mg of GFP–His_8 and incubated for 3 h at 4˚C after addition of 10 mM imidazole. Slurry was loaded onto a glass Econo-Column (Bio-Rad) and washed in 1 x PBS buffer containing 0.1% DDM, 150 mM NaCl for 3 x 10 column volumes at 10, 20 and 45 mM imidazole concentrations, respectively. The NapA-GFP-His_8 fusion was eluted in two column volumes of 1 x PBS buffer containing 0.6% nonyl-β-D-maltopyranoside (NM; Generon), 150 mM NaCl and 250 mM imidazole. The eluted protein was dialysed overnight in the

presence of stoichiometric amounts of His_6-tagged TEV protease containing 5 mM DTT, in 3 l of buffer containing 20 mM Tris-HCl, pH 7.5, 150 mM NaCl and 0.5% NM. Dialysed sample was passed through a 5 ml Ni-NTA His-Trap column (GE Healthcare), and the flow-through containing NapA was collected. Protein was concentrated using concentrators with a relative molecular mass cut-off of 100 kilodalton (kDa). To re-oxidise all proteins to a similar level for functional studies, the purified proteins were incubated with 1 mM $CuSO_4$ for 30 min prior loading onto a Superdex 200 10/300 gel filtration column (GE Healthcare) equilibrated in buffer containing 20 mM Tris-HCl, pH 7.5, 150 mM NaCl and 0.03% DDM. For structural investigation, the protein was not incubated with $CuSO_4$, but rather loaded directly onto a Superdex 200 10/300 gel filtration column (GE Healthcare) equilibrated in buffer containing 20 mM Tris-HCl, pH 7.5, 150 mM NaCl and 0.6% NM.

Na^+/H^+ cysteine accessibility. To probe for cysteine accessibility 5 µg of either purified NapA wild type or cysteine mutants thereof were incubated with 5 mM mPEG-5K (methoxypolyethylene glycol maleimide; Sigma) at room temperature for 45 min. Incubated proteins were analysed for reactivity by a shift in size after electrophoresis on 12% NuPAGE-gels (Invitrogen) and staining by Coomassie. Cysteine accessibility was further assessed by incubating 10 µg of either purified NapA wild type or cysteine mutants thereof with 2 µg of CPM (7-Diethylamino-3-(4'-Maleimidylphenyl)-4-Methylcoumarin; Life Technologies) dye at 40 °C for 15 min. Samples were subjected to SDS-PAGE and the in-gel fluorescent band intensity (blue light: 480 nm) use to quantify level of free sulfhydryl groups. Original images of gels used in this study can be found in Supplementary Data Set 1.

Na^+/H^+ antiport activity Na^+/H^+ antiport activity in proteoliposomes was carried out as described previously [6]. In brief, L-α-Phosphatidylcholine lipids (Sigma) were diluted to 10 mg/ml with 10 mM MOPS, pH 6.5, 5 mM $MgCl_2$, 100 mM KCl (MMK) at pH 6.5 and vortexed until uniformity. Lipids underwent 8 cycles of freeze-thawing and stored at -80 °C until required. Prior to reconstitution, liposomes were extruded through polycarbonate filters (200 nm) and destabilized by addition of sodium

cholate to a final concentration of v/v 0.65%. Either 100 µg of purified NapA or cysteine mutants thereof were co-reconstituted together with 100 µg of purified *E. coli* F_oF_1 ATP synthase in MMK buffer (10 mM MOPS-NaOH, pH 8.0, 5.0 mM $MgCl_2$, 100 mM KCl) as described previously [6,36,37]. Typically, 50 µL proteoliposomes were diluted into 1.5 mL MMK buffer containing 2.5 nM 9-aino-6-chloro-2-methoxyacridine (ACMA) and 130 nM valinomycin. Fluorescence was monitored at 480 nm using an excitation wavelength of 410 nm in a fluorescence spectrophotometer (Cary Eclipse, Agilent Technologies). An outward-directed pH gradient (acidic inside) was established by the addition of final v/v 0.2 mM ATP, as followed by a change in ACMA fluorescence. After ~3 min equilibration, the activity of NapA wild type and mutants thereof was assessed by the dequenching of ACMA fluorescence after addition of the indicated concentrations of NaCl or LiCl. Addition of 20 mM NH_4Cl leads to near complete dequenching. The apparent affinity K_M for Na^+ or Li^+ was measured at the indicated concentrations in the presence or absence of 5 mM dithiothreitol (DTT). The data were fitted from duplicate measurements to the Michaelis–Menten equation by nonlinear regression using the GRAPHPAD PRISM software. The K_M values reported are the mean ± s.e.m. of the fit.

To assess the propensity for disulfide-bond formation antiport activity for NapA wild type, single and double-cysteine mutants were first assessed in MMK buffer containing 5 mM DTT essentially as described above, after the addition of saturating 10 mM $LiCl_2$. DTT was removed from proteoliposomes containing either wild type NapA or cysteine mutants by their passage through two G-25 columns (GE Healthcare). Antiport activities, under these “non-reducing” conditions, were re-assessed using the equivalent amount of proteoliposomes by the addition of saturating, 10 mM $LiCl_2$ in MMK buffer without DTT. To confirm that the loss of antiport activity for the double-cysteine mutant was because of disulfide-bond formation rather than a loss of sample, DTT was further added back to proteoliposomes where it had been removed. Each experiment was performed three times from three independent purifications. The data shown represent the s.e.m.

from three technical repeats from one of the three independent experiments.

Isothermal calorimetry. All measurements were made on a Micro-200 ITC (MicroCal, Malvern), similar to the experimental setup previously described for NhaA[7]. 150 µl of the double-cysteine V31C I130C mutant at 300 µM was diluted to 2 mL in 50 mM Bis-tris-propane, 150 mM KCl, 0.03% DDM buffer at the desired pH and concentrated to ~150 µl using concentrators with a relative molecular cut-off of 100 kDa. This washing step was repeated a minimum of 6 times. The last flow through was used to dilute a 2M stock solution of LiCl or NaCl and the protein to the concentrations used for the runs. Disulfide-bond formation was confirmed after these steps by the maleimide-PEG shift assay and ACMA transport assay both before and after the ITC run. Protein at 90-150 µM was loaded into the sample cell and 15 mM LiCl or 40 mM NaCl in the injection syringe. The system was equilibrated to 20 ˚C with a stirring speed of 600 rpm. Titration curves were initiated by a 0.5 µl injection followed by 2 µl or 2.8 µl injections every 200 s. Background corrections were obtained by injecting LiCl or NaCl into buffer and buffer into protein with the same parameters. ORIGIN 7 was used to integrate, correct and normalize the heat for each injection and fit them to a single-site binding isotherm using a fixed protein/ligand stoichiometry of 1 and excluding the peak from the first injection.

Crystallization and diffraction. Crystals of the double-cysteine V31C I130C mutant were grown at 20˚C using the hanging drop vapour diffusion method. 1.2 µl of protein at 15 mg/ml was mixed 1:1 with reservoir solution containing 50 mM glycine pH 9.5, 0.1M NaCl, 34-38% PEG 300. Crystals were dehydrated in 36–40% PEG 300 (2% increment overnight) followed by flash freezing in liquid nitrogen before data collection.

For crystallization of NapA in lipidic mesophases the triple cysteine mutant (M20C V166C V326C) that was used for determining the previously published outward-facing structure (4bwx) further shown to have wild type-like activity [6], was purified and concentrated to 30 mg/mL and mixed with 7.7 MAG (Lot: 141MG(7.7)-15, Avanti) using a coupled syringe-mixing device to form the cubic phase at a

protein solution:lipid weight ratio of 1:1. Crystallization trials were set up by dispensing 50 nL cubic phase onto 96-well Laminex glass plate (MD11-50, Molecular Dimensions), which was then covered with 800 nL of precipitant solution 0.1 M MES pH 6.5, 0.1 M NaSCN, 40 %(v/v) PEG 400 using a Mosquito LCP robot (TTP Labtech). After sealing with Laminex glass cover (MD11-52, Molecular Dimensions), the plates were stored at 20˚C.

Structure determination. Data were collected at Diamond Light Source. Diffraction data were indexed and integrated with XDS [38] and scaled with Aimless [39]. Initial phase were obtained by molecular replacement in Phenix [40] (autoMR) using the dimer domain of NapA (4bwz model) and the core domain as separate search models. Refinement was carried out in Autobuster [41]/Phenix [40] and manual rebuilding in Coot [42]. One TLS group was used during the refinement of the inward-facing conformation. The quality of the model was assessed by Molprobity [43] throughout this process. All residues from final models are found in allowed region of the ramachandran plot and both structures are ranked in the 100th percentile by the Molprobity server.

Structure Analysis. Superimposition, figures and movies were generated by Pymol [44]. The program O [45] was used to calculate the angle through which the Core domain of the inward-facing structure needs to rotate to be superposed on the same domain of the inward-facing structure after the respective structures have been superposed on their dimer domains. For this analysis the domains were first superposed in LSQMAN [46] such that all matching Cα pairs were less than 3.8 Å apart after superposition. To visualise the positional sequence conservation in NapA outward- and inward-facing structures the ConSurf server was used with default settings[47].

Molecular dynamics simulations. All-atom, explicit solvent MD simulations were performed with Gromacs 4.6.5 [48] and the CHARMM36 force field for the protein with the CMAP correction [49-51], ions and lipids [52] together with the CHARMM TIP3P water model [49]. The NapA dimer was simulated in a ~4:1 ratio 1-palmitoyl-2-

oleoylphosphatidylethanolamine (POPE)/1-palmitoyl-2-oleoylphosphatidylglycerol (POPG) bilayer. Simulations of the outward facing structure were based on the LCP crystal structure. Simulations were also performed with the inward facing disulfide-linked V31C I130C structure and an inward facing model of the wild type protein that was obtained by changing C31 back to V31 and C130 to I130. Simulations were run for 1 μs. Wild type simulations were independently repeated twice for 0.3 μs, starting from the same initial system conformation but using differing random number seeds. All simulations are summarized in Supplementary Table 1.

Protein structures were embedded into the model membrane with a coarse-grained self-assembly protocol [53] and subsequent conversion of the lipids to an all-atom representation [54] as described for our previous simulations of NapA [6]. The total system consisted of about 120,000 atoms in an orthorhombic simulation cell with a free NaCl concentration of ~250 mM. Most titratable residues were simulated in their default charge states as predicted by PROPKA 3.1 [55] for pH 7.8, which includes charged forms of the residues D156 and K305 near the ion binding site. The binding site residue D157 was simulated in its charged form in the IF and OF conformation, despite a prediction of a neutral charge state in the OF conformation because our previous work suggested that it would be charged (deprotonated) when a sodium/proton antiporter binds a Na^+ ion [5,6].

Equilibrium MD simulations were performed after energy minimization and ~15 ns of equilibration with position restraints (harmonic force constant 1000 kJ mol^{-1} nm^{-2} on all heavy protein atoms). All simulations were carried out under periodic boundary conditions at constant temperature T=310 K and pressure P=1 bar. The velocity rescaling thermostat [56] was employed with a time constant of 1 ps and three separate temperature-coupling groups for protein, lipids and solvent. The Parrinello-Rahman barostat [57] with time constant 5 ps and compressibility 4.6×10^{-5} bar^{-1} was used for semi-isotropic pressure coupling. The Verlet neighbour list with a cut-off of 1.2 nm was updated every 20 steps. Coulomb interactions were calculated with the smoothed particle mesh Ewald (SPME) method [58] with a real-space cut-off

of 1.2 nm while interactions beyond the cut-off were calculated in reciprocal space with a fast Fourier transform on a grid with 0.12 nm spacing and 4th order spline interpolation. The Lennard-Jones potential was shifted to zero at a cut-off of 1.2 nm, without applying any dispersion corrections [59]. Bonds to hydrogen atoms were constrained with the P-LINCS algorithm [60] (using an expansion order of four and two LINCS iterations) or SETTLE [61] (for water molecules). The classical equations of motions were integrated with the leapfrog algorithm with a time step of 2 fs.

Non-bonded parameters for lipid simulations can be critical and artefacts have been reported with wrong choices of these parameters [59]. We carefully selected a set of parameters that is compatible with the Verlet neighbour list scheme in Gromacs (which is required for running on GPUs and high performance with the CHARMM TIP3P water model on conventional hardware) while remaining close to the original values of the CHARMM force field. The simulation parameters were validated with simulations of pure POPC (used for validation instead of POPG) and POPE bilayers of 288 lipids and 50 water molecules per lipid for ~250 ns length that gave areas per lipid within 1 Å^2 (POPC) and 3 Å^2 (POPE) of the original CHARMM36 values [52] (data not shown). Furthermore, our values differ from the experimental areas per lipid by no more than 2 Å^2, indicating that our parameter settings in Gromacs produce results of similar quality to the native simulations in CHARMM.

Analysis of molecular dynamics simulations. MD simulations were analysed with code based on MDAnalysis [62] (http://www.mdanalysis.org) and MDSynthesis (https://github.com/datreant/MDSynthesis). The movement of domains was assessed in the coordinate system associated with the membrane. In the MD simulations, the average normal of the bilayer was parallel to the *z*-axis of the fixed simulation coordinate system and hence we performed all calculations with the *z* coordinates of the centers of mass of the core and dimer domain and the bilayer itself. Probability distributions $f_Z(z)$ of a coordinate Z were calculated as Gaussian kernel density estimates (KDE) from the raw simulation data (obtained at 1 ps intervals). The kernel width of the KDE was chosen according to Scott's criterion as

implemented in the scipy.stats.gaussian_kde() function from the SciPy package (http://www.scipy.org). The joint difference distribution of the random variable ΔZ = Z_{OF} – Z_{IF} was calculated as the convolution $f(\mathbf{\Delta}Z) = \int dz\, f_Z^{OF}(z)\; f_Z^{IF}(z - \mathbf{\Delta}Z)$. In order to calculate the z-shift of the core domain relative to the dimer domain between the two crystal structures it is still necessary to orient the two structures relative to the membrane. We performed the orientation of the crystal structures in two different ways. (1) The dimer domain was superimposed on frames from the MD simulations, distributions of the z position and the relative shift were calculated as described, yielding ΔZ = 7.2±1.1 Å (standard deviation). (2) The dimer domain was superimposed on the oriented OF NapA structure (PDB: 4BWZ) as provided by the Orientation of Proteins in the Membrane database (OPM, http://opm.phar.umich.edu/)[63] which uses an electrostatic model and a simple low-dielectric model for the membrane. This static picture yields ΔZ = 7.1 Å, in full agreement with the analysis based on the orientation of the NapA dimer in the explicit membrane the MD simulations.

Binding of Na^+ ions was assessed with a distance criterion: Any Na^+ ion within 3 Å of any carboxyl oxygen atom of either D157 or D156 was considered bound, i.e., an ion was considered bound if it contained one of the aspartate carboxylates in its first coordination shell. The probability for observing at least one ion within 3 Å of any of the O_δ of D157 or D156, P_{bound}, shown in Supplementary Figure 4 and Supplementary Table 2 was calculated as the bound time divided by the total simulated time. In order to better estimate P_{bound} we independently repeated simulations an additional two times for 300 ns. However, small but infrequent conformational changes such as movements of parts of helices 4 and 11 affect binding site accessibility and binding (e.g. the absence of any binding in protomer B in the inward facing conformation in the 1 μs simulation as shown in Supplementary Table 2). Such infrequent events are not well sampled, even in 1 μs of simulation. We therefore decided to weigh all simulations equally for the purpose of computing averages of P_{bound} over different initial conditions (Supplementary Fig. 4) and

therefore only used the first 300 ns of the 1-μs simulations together with the full 300 ns of the two repeats. For the analysis of coordination geometry, all trajectory frames were used that contained a bound Na^+ ion. The ion-oxygen radial distribution function was computed from all oxygen atoms (protein and water) within 10 Å of the ion. Per-residue contributions (where all water molecules count as identical) to the first coordination shell number (oxygen atoms within 3 Å of the ion) were computed as the total residence time of the oxygen in the first solvation shell divided by the total time that an ion was bound.

Images showing simulation data were prepared with VMD [64] and the Bendix plugin [65].

Methods References

34. Wagner, S. et al. Tuning *Escherichia coli* for membrane protein overexpression. *Proc Natl Acad Sci U S A* **105**, 14371-6 (2008).
35. Lee, C. et al. MemStar: a one-shot *Escherichia coli*-based approach for high-level bacterial membrane protein production. *FEBS Lett* **588**, 3761-9 (2014).
36. Ishmukhametov, R.R., Galkin, M.A. & Vik, S.B. Ultrafast purification and reconstitution of His-tagged cysteine-less Escherichia coli F1Fo ATP synthase. *Biochim Biophys Acta* **1706**, 110-6 (2005).
37. Wiedenmann, A., Dimroth, P. & von Ballmoos, C. Functional asymmetry of the F(0) motor in bacterial ATP synthases. *Mol Microbiol* **72**, 479-90 (2009).
38. Kabsch, W. XDS. *Acta Crystallogr D* **66**, 125-132 (2010).
39. Evans, P.R. & Murshudov, G.N. How good are my data and what is the resolution? *Acta Crystallogr D Biol Crystallogr* **69**, 1204-14 (2013).
40. Adams, P.D. et al. PHENIX: a comprehensive Python-based system for macromolecular structure solution. *Acta Crystallographica Section D* **66**, 213-221 (2010).
41. Bricogne, G. et al. BUSTER. (Global Phasing, Cambridge, UK, 2011).
42. Emsley, P. & Cowtan, K. Coot: model-building tools for molecular graphics. *Acta Crystallographica Section D* **60**, 2126-2132 (2004).
43. Davis, I.W., Murray, L.W., Richardson, J.S. & Richardson, D.C. MOLPROBITY: structure validation and all-atom contact analysis for nucleic acids and their complexes. *Nucleic Acids Res* **32**, W615-9 (2004).
44. Delano, W.L. The PyMOL Molecular Graphics System. *DeLano Scientific, Palo Alto, CA, USA* (2002).
45. Jones, T.A. & Kjeldgaard, M. Electron-density map interpretation. *Methods Enzymol* **277**, 173-208 (1997).
46. Jones, G.J.K.a.T.A. A super position. . *CCP4/ESF-EACBM Newsletter on Protein Crystallography* **31**, 9-14 (1994).
47. Landau, M. et al. ConSurf 2005: the projection of evolutionary conservation scores of residues on protein structures. *Nucleic Acids Res* **33**, W299-302 (2005).
48. Pronk, S. et al. GROMACS 4.5: a high-throughput and highly parallel open source molecular simulation toolkit. *Bioinformatics* **29**, 845-54 (2013).
49. MacKerell, A. et al. All-atom empirical potential for molecular modeling and dynamics studies of proteins. *J Phys Chem B* **102**, 3586--3616 (1998).
50. MacKerell, J., A. D., Feig, M. & Brooks III, C.L. Extending the treatment of backbone energetics in protein force fields: limitations of gas-phase quantum mechanics in reproducing protein

conformational distributions in molecular dynamics simulations. *J Comp Chem* **25**, 1400--1415 (2004).
51. Best, R.B. et al. Optimization of the additive CHARMM all-atom protein force field targeting improved sampling of the backbone ϕ, ψ and side-chain $\chi(1)$ and $\chi(2)$ dihedral angles. *J Chem Theory Comput* **8**, 3257-3273 (2012).
52. Klauda, J.B. et al. Update of the CHARMM all-atom additive force field for lipids: validation on six lipid types. *J Phys Chem B* **114**, 7830-43 (2010).
53. Scott, K.A. et al. Coarse-grained MD simulations of membrane protein-bilayer self-assembly. *Structure* **16**, 621–630 (2008).
54. Stansfeld, P.J. & Sansom, M.S.P. From Coarse Grained to Atomistic: A Serial Multiscale Approach to Membrane Protein Simulations. *J Chem Theo Comp* **7**, 1157-1166 (2011).
55. Søndergaard, C.R., Olsson, M.H.M., Rostkowski, M. & Jensen, J.H. Improved Treatment of Ligands and Coupling Effects in Empirical Calculation and Rationalization of pKa Values. *Journal of Chemical Theory and Computation* **7**, 2284-2295 (2011).
56. Bussi, G., Donadio, D. & Parrinello, M. Canonical sampling through velocity rescaling. *J Chem Phys* **126**, 01410 (2007).
57. Parrinello, M. & Rahman, A. Polymorphic transitions in single crystals: A new molecular dynamics method. *J Appl Phys* **52**, 7182-7190 (1981).
58. Essman, U. et al. A smooth particle mesh Ewald method. *J Chem Phys* **103**, 8577--8592 (1995).
59. Piggot, T.J., Piñeiro, Á. & Khalid, S. Molecular Dynamics Simulations of Phosphatidylcholine Membranes: A Comparative Force Field Study. *J Chem Theo Comput* **8**, 4593--4609 (2012).
60. Hess, B. P-LINCS: A Parallel Linear Constraint Solver for Molecular Simulation. *J Chem Theo Comp* **4**, 116--122 (2008).
61. Miyamoto, S. & Kollman, P.A. SETTLE: An Analytical Version of the SHAKE and RATTLE Algorithms for Rigid Water Models. *J Comp Chem* **13**, 952--962 (1992).
62. Michaud-Agrawal, N., Denning, E.J., Woolf, T.B. & Beckstein, O. MDAnalysis: A Toolkit for the Analysis of Molecular Dynamics Simulations. *J Comp Chem* **32**, 2319–2327 (2011).
63. Lomize, M.A., Lomize, A.L., Pogozheva, I.D. & Mosberg, H.I. OPM: orientations of proteins in membranes database. *Bioinformatics* **22**, 623-5 (2006).
64. Humphrey, W., Dalke, A. & Schulten, K. VMD — Visual Molecular Dynamics. *J Mol Graph* **14**, 33–38 (1996).
65. Dahl, A.C.E., Chavent, M. & Sansom, M.S.P. Bendix: Intuitive helix geometry analysis and abstraction for VMD. *Bioinformatics* **28**, 2193–2194 (2012).

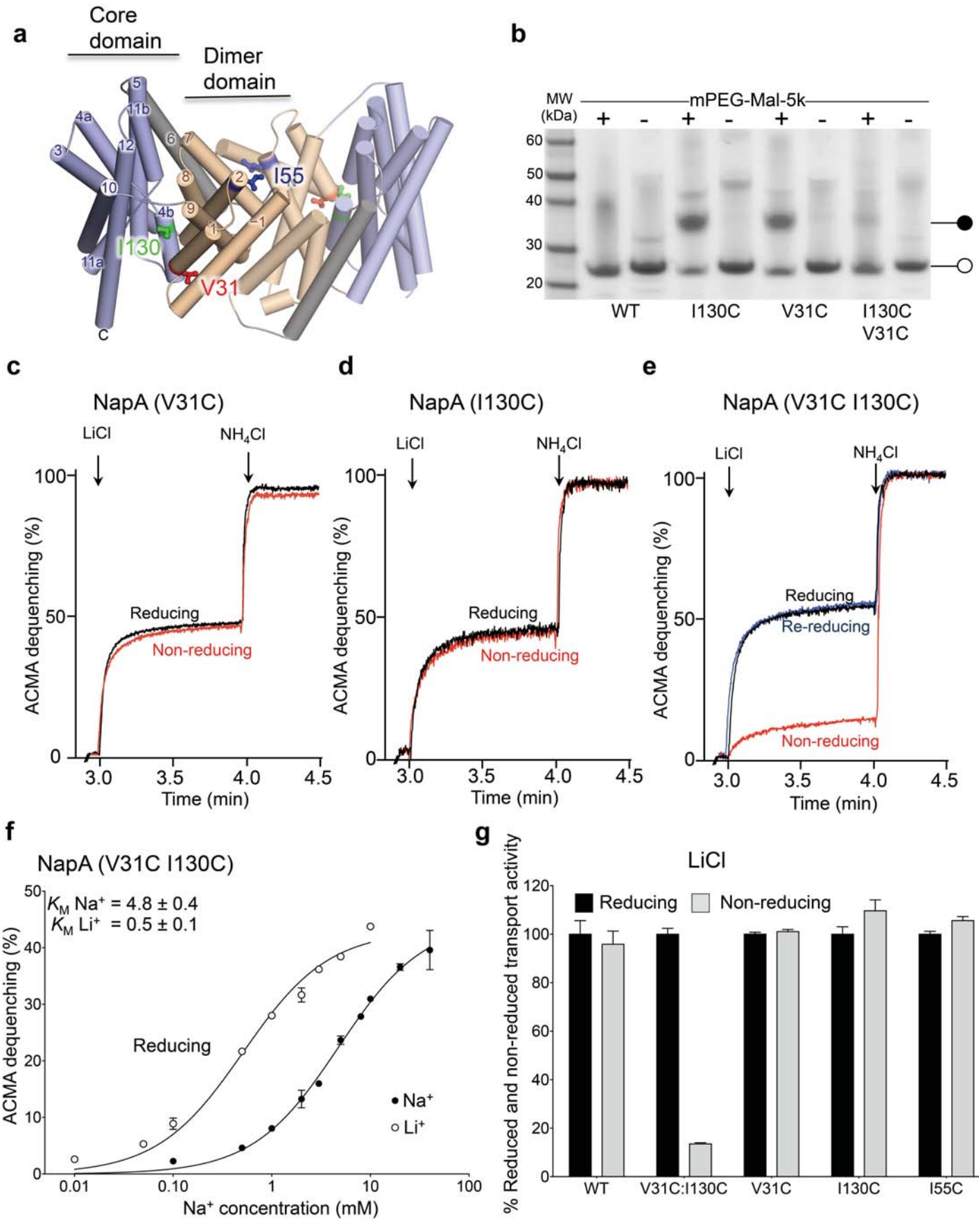
a
Core domain
Dimer domain
I55
I130
V31
C
b
MW (kDa)
mPEG-Mal-5k
+ - + - + - + -
60
50
40
30
20
WT
I130C
V31C
I130C V31C
c
NapA (V31C)
LiCl
NH4Cl
ACMA dequenching (%)
Reducing
Non-reducing
Time (min)
d
NapA (I130C)
e
NapA (V31C I130C)
Re-reducing
f
NapA (V31C I130C)
KM Na+ = 4.8 ± 0.4
KM Li+ = 0.5 ± 0.1
Na+ concentration (mM)
g
LiCl
Reducing
Non-reducing
% Reduced and non-reduced transport activity
WT
V31C:I130C
V31C
I130C
I55C

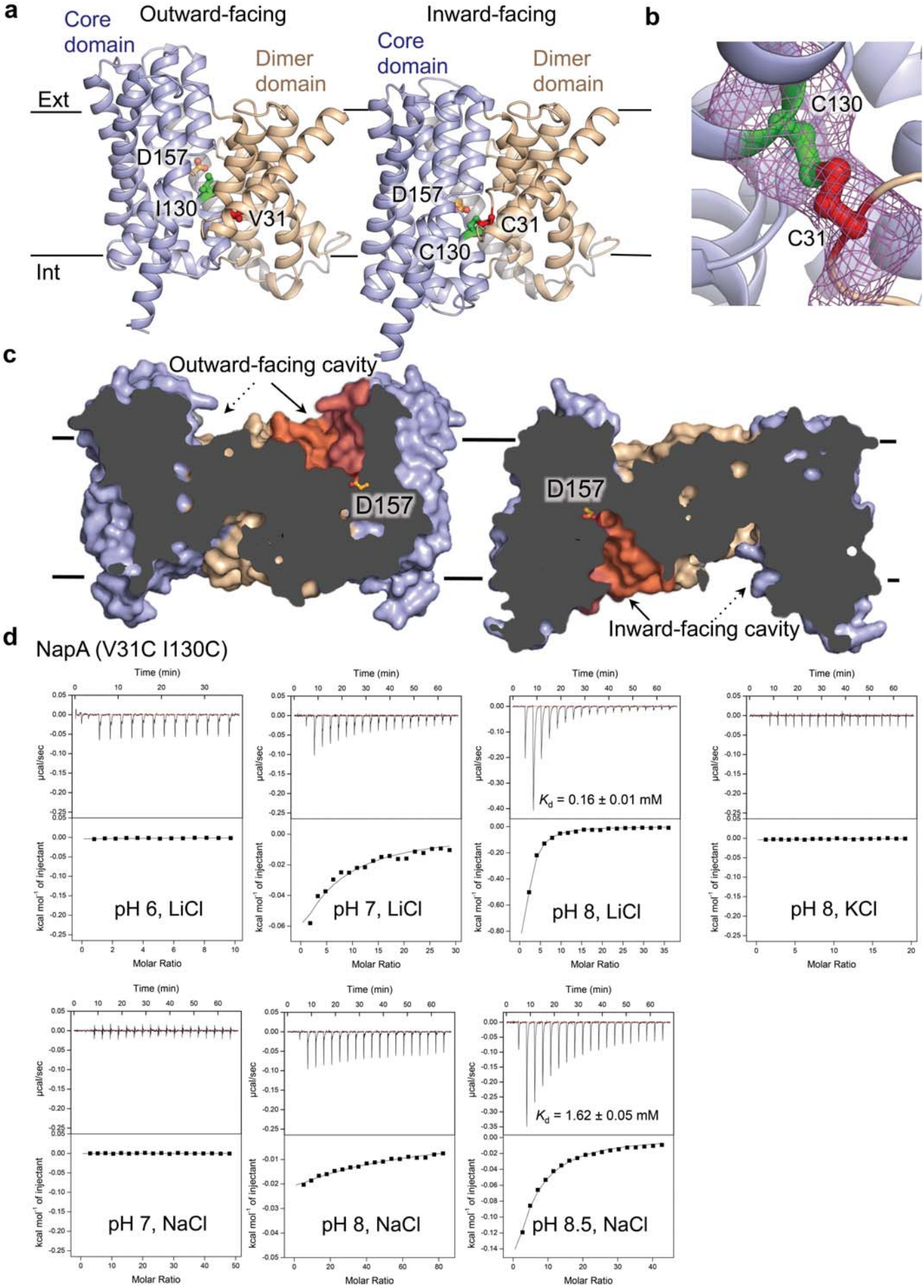
a
Outward-facing
Inward-facing
Core domain
Dimer domain
Core domain
Dimer domain
Ext
Int
D157
I130
V31
D157
C31
C130
b
C130
C31
c
Outward-facing cavity
D157
D157
Inward-facing cavity
d
NapA (V31C I130C)
Time (min)
µcal/sec
kcal mol⁻¹ of injectant
Molar Ratio
pH 6, LiCl
pH 7, LiCl
K_d = 0.16 ± 0.01 mM
pH 8, LiCl
pH 8, KCl
pH 7, NaCl
pH 8, NaCl
K_d = 1.62 ± 0.05 mM
pH 8.5, NaCl

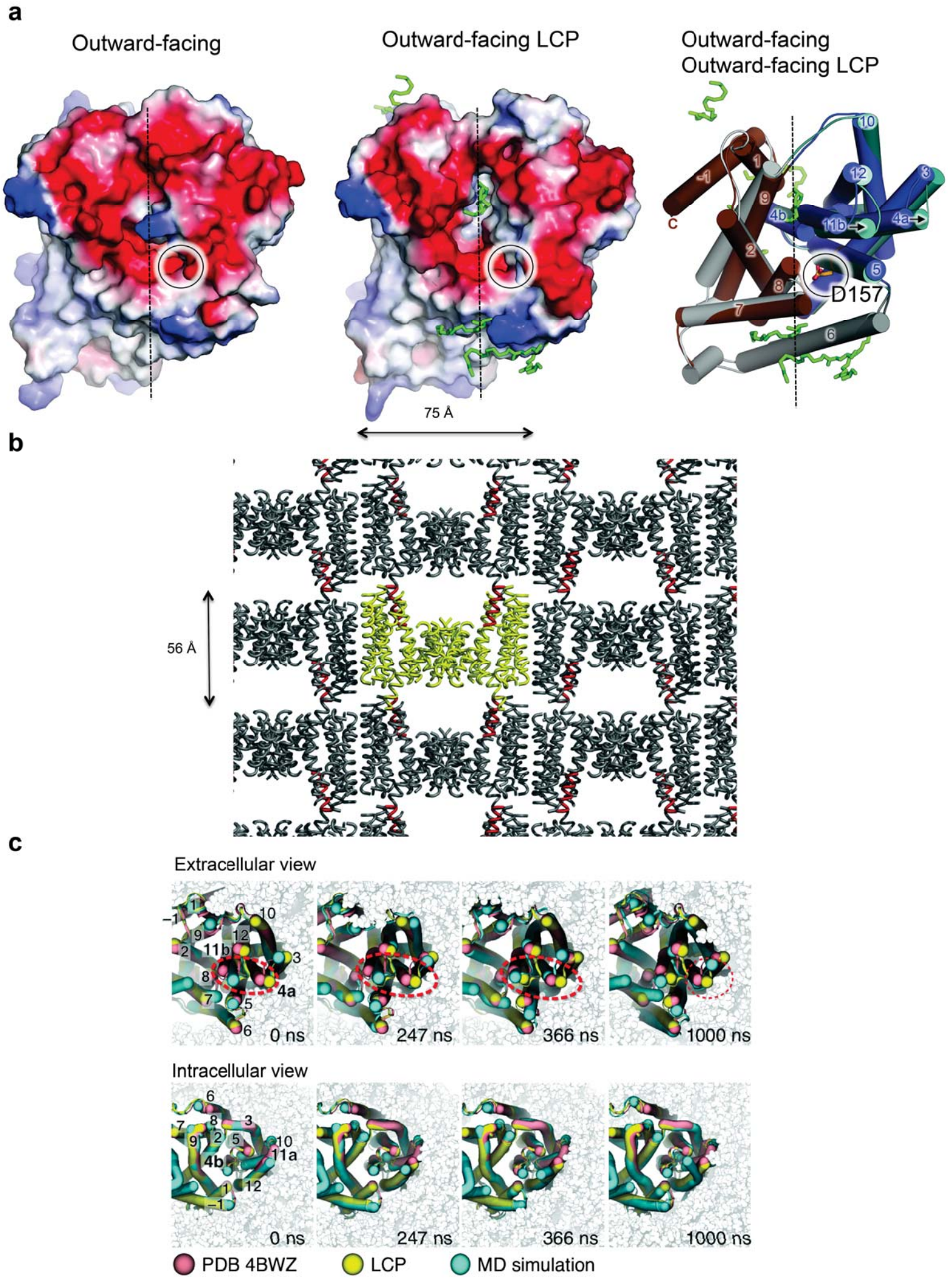
a
Outward-facing
Outward-facing LCP
Outward-facing
Outward-facing LCP
75 Å
D157
b
56 Å
c
Extracellular view
0 ns
247 ns
366 ns
1000 ns
Intracellular view
0 ns
247 ns
366 ns
1000 ns
PDB 4BWZ
LCP
MD simulation

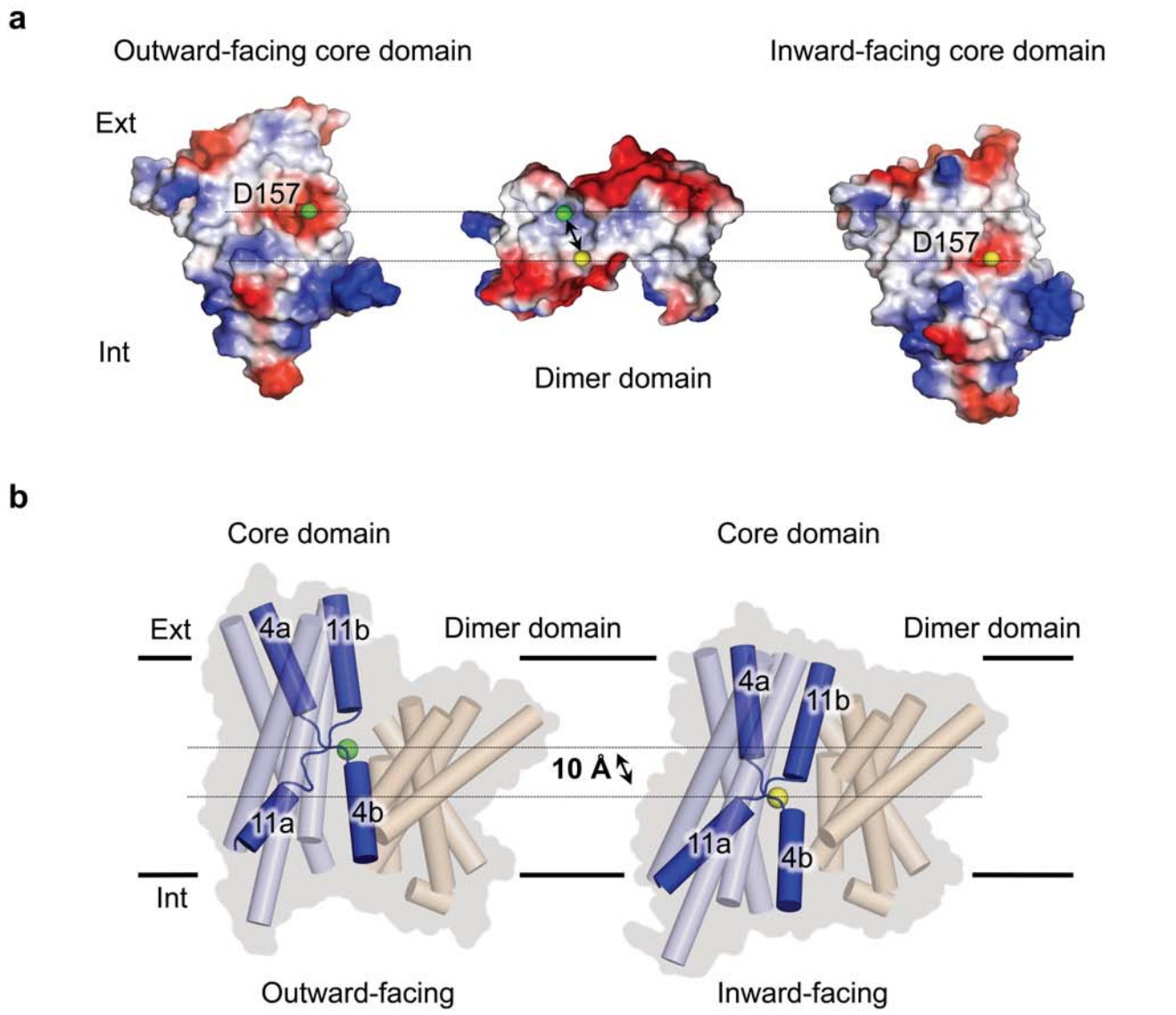
a
Outward-facing core domain
Inward-facing core domain
Ext
D157
Int
Dimer domain
D157
b
Core domain
Core domain
Ext
4a
11b
Dimer domain
Dimer domain
10 Å
11a
4b
Int
4a
11b
11a
4b
Outward-facing
Inward-facing
c
0.40 Å
(134)
0.66 Å
(154)
0.57 Å
(124)
1.4Å
(180)
0.57 Å
(124)
0.95 Å
(185)
Outward-facing
Outward-facing LCP
Outward-facing LCP
Inward-facing
Outward-facing
Inward-facing

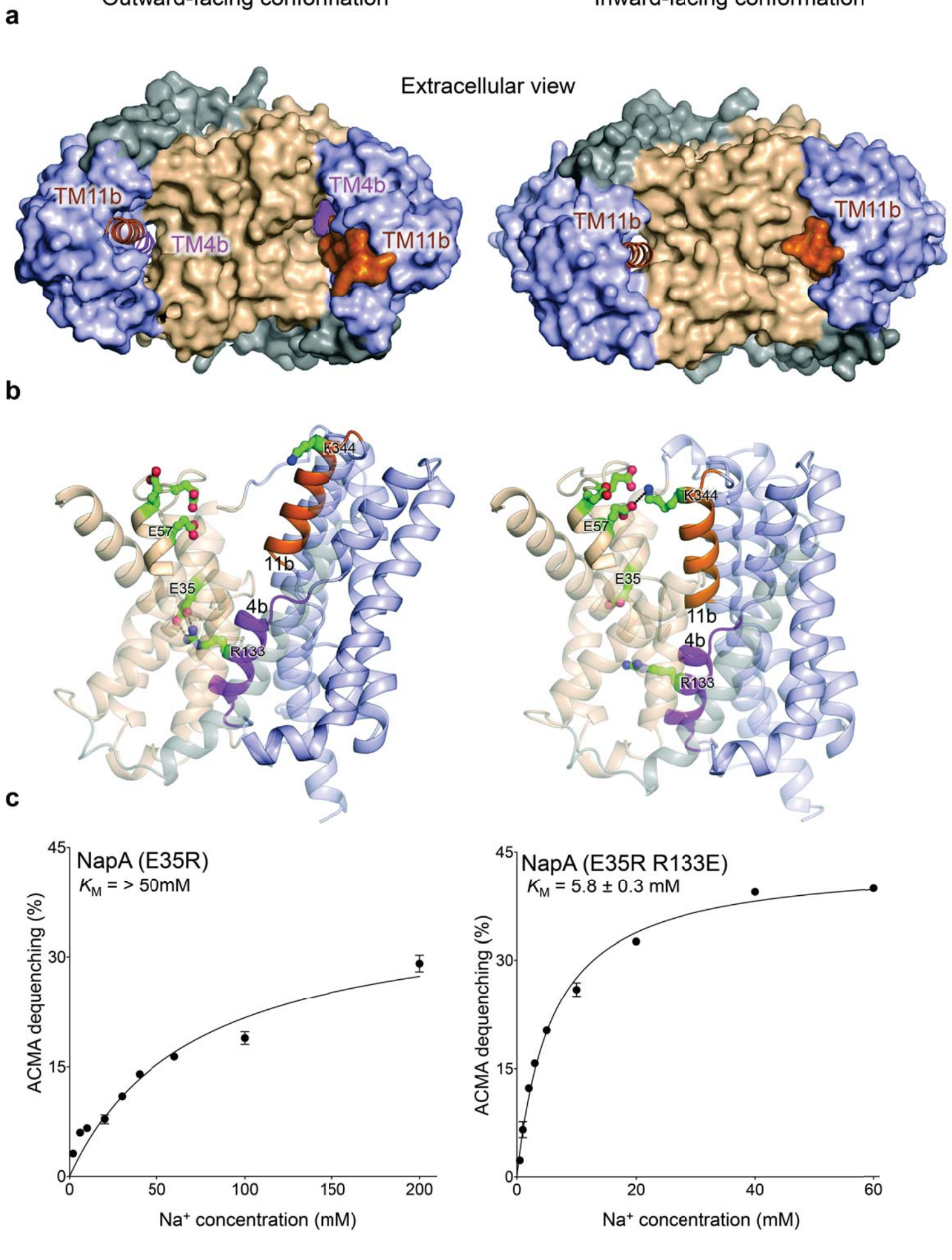
a
Outward-facing conformation
Inward-facing conformation
Extracellular view
TM11b
TM4b
TM4b
TM11b
TM11b
TM11b
b
K344
E57
11b
E35
4b
R133
K344
E57
E35
11b
4b
R133
c
NapA (E35R)
K_M = > 50mM
ACMA dequenching (%)
Na+ concentration (mM)
NapA (E35R R133E)
K_M = 5.8 ± 0.3 mM
ACMA dequenching (%)
Na+ concentration (mM)

a

Rocking-bundle alternating-access mechanism

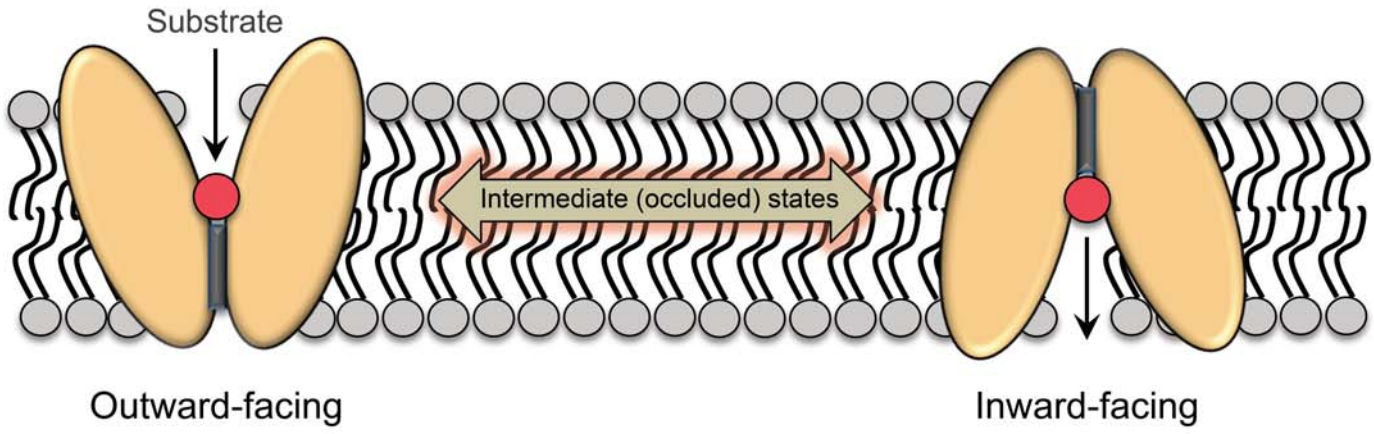

b

Elevator alternating-access mechanism